(12) INTERNATIONAL APPLICATION PUBLISHED UNDER THE PATENT COOPERATION TREATY (PCT)

(19) World Intellectual Property Organization
International Bureau

(43) International Publication Date
09 January 2025 (09.01.2025)

WIPO | PCT

(10) International Publication Number
WO 2025/010333 A2

(51) International Patent Classification:
A61B 6/03 (2006.01)

(21) International Application Number: PCT/US2024/036703

(22) International Filing Date: 03 July 2024 (03.07.2024)

(25) Filing Language: English

(26) Publication Language: English

(30) Priority Data:
63/524,955 05 July 2023 (05.07.2023) US
63/662,475 21 June 2024 (21.06.2024) US

(71) Applicant: RENSSELAER POLYTECHNIC INSTITUTE [US/US]; 110 8th Street, J Building, Troy, NY 12180 (US).

(72) Inventors: LI, Mengzhou; 59 25th Street, Troy, NY 12180 (US). **WANG, Ge**; 20 Hilander Drive, Loudonville, NY 12211 (US).

(74) Agent: GANGEMI, Anthony, P.; Barclay Damon LLP, 545 Long Wharf Drive, 9th Floor, New Haven, CT 06511 (US).

(81) Designated States *(unless otherwise indicated, for every kind of national protection available)*: AE, AG, AL, AM, AO, AT, AU, AZ, BA, BB, BG, BH, BN, BR, BW, BY, BZ, CA, CH, CL, CN, CO, CR, CU, CV, CZ, DE, DJ, DK, DM, DO, DZ, EC, EE, EG, ES, FI, GB, GD, GE, GH, GM, GT, HN, HR, HU, ID, IL, IN, IQ, IR, IS, IT, JM, JO, JP, KE, KG, KH, KN, KP, KR, KW, KZ, LA, LC, LK, LR, LS, LU, LY, MA, MD, MG, MK, MN, MU, MW, MX, MY, MZ, NA, NG, NI, NO, NZ, OM, PA, PE, PG, PH, PL, PT, QA, RO, RS, RU, RW, SA, SC, SD, SE, SG, SK, SL, ST, SV, SY, TH, TJ, TM, TN, TR, TT, TZ, UA, UG, US, UZ, VC, VN, WS, ZA, ZM, ZW.

(84) Designated States *(unless otherwise indicated, for every kind of regional protection available)*: ARIPO (BW, CV, GH, GM, KE, LR, LS, MW, MZ, NA, RW, SC, SD, SL, ST, SZ, TZ, UG, ZM, ZW), Eurasian (AM, AZ, BY, KG, KZ, RU, TJ, TM), European (AL, AT, BE, BG, CH, CY, CZ, DE, DK, EE, ES, FI, FR, GB, GR, HR, HU, IE, IS, IT, LT, LU, LV, MC, ME, MK, MT, NL, NO, PL, PT, RO, RS, SE, SI, SK, SM, TR), OAPI (BF, BJ, CF, CG, CI, CM, GA, GN, GQ, GW, KM, ML, MR, NE, SN, TD, TG).

Published:
— *without international search report and to be republished upon receipt of that report (Rule 48.2(g))*

(54) Title: MOTION CORRECTION WITH LOCALLY LINEAR EMBEDDING FOR COMPUTED TOMOGRAPHY

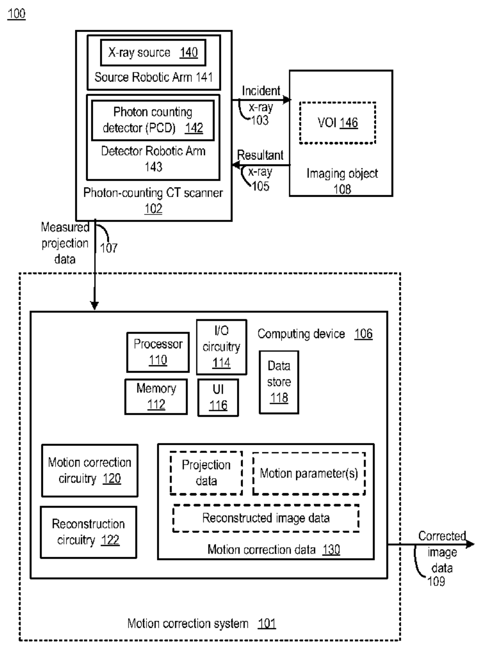

FIG. 1

(57) Abstract: A CT apparatus in which the x-ray source is coupled to a source robotic arm and the detector is coupled to a detector robotic arm. A motion correction module utilizes a locally linear embedding motion correction algorithm with normalized cross correlation to estimate the geometric parameters associated with the positions of the source and detector and the angle of the detector. These estimates are used to reconstruct the image data and produce corrected images with fewer errors resulting from patient movement, misalignments, and coordination issues in the system.

WO 2025/010333 A2

MOTION CORRECTION WITH LOCALLY LINEAR EMBEDDING FOR COMPUTED TOMOGRAPHY

CROSS REFERENCE TO RELATED APPLICATION(S)

This application claims the benefit of U.S. Provisional Application No. 63/524,955, filed July 5, 2023 and U.S. Provisional Application No. 63/662,475 filed June 21, 2024, each of which are incorporated by reference as if disclosed herein in their entireties.

GOVERNMENT LICENSE RIGHTS

This invention was made with government support under award number CA237267 awarded by the National Institutes of Health. The government has certain rights in the invention.

FIELD

The present disclosure relates to motion correction with locally linear embedding, and more particularly, to motion correction with locally linear embedding for computed tomography (CT) that involves truncated projection data.

BACKGROUND

Robot arm-based CT is finding increasing utility in industrial applications and are now finding applications in biomedical imaging, especially for interior tomography. Developments in high-resolution (HR) photon-counting detectors (PCDs) and high-power micro-focus X-ray tubes have made ultrahigh-resolution (UHR) interior CT feasible for in vivo imaging. Such an UHR micro-CT system is useful for various clinical applications, including plaque characterization, temporal bone imaging, lung nodule detection, bone modeling, and others. However, as spatial resolution increases, the challenges of image artifacts become more pronounced, arising from patient movement, minor system misalignment, and robot coordination errors.

Thus, improved resolution in CT challenges the traditional assumptions about the smoothness of patient motion or geometric errors over projection views, which has underpinned most existing motion compensation methods.

SUMMARY

According to a first aspect of the present technology, a computed tomography (CT) apparatus is provided that includes an x-ray source, an x-ray detector adapted to output scan data of a volume of interest (VOI) contained in an imaging object, and a computing device.

The computing device comprises a motion correction circuitry that includes software instructions for: estimating a set of geometric parameters comprising the relative position of the x-ray source, the relative position of the x-ray detector, and the relative angular orientation of the x-ray detector based on the scan data and utilizing a locally linear embedding (LLE) motion correction algorithm wherein a set of weights for representing each of the set of geometric parameters is optimized by maximizing the normalized cross correlation between the scan data and its embedding; generating, via a reconstruction module, reconstructed image data from the estimated geometric parameters; and outputting corrected image data based, at least in part, on the reconstructed image data, to form a corrected image of the VOI. In some embodiments, the x-ray source is coupled to a source robotic arm and in some embodiments, the x-ray detector is coupled to a detector robotic arm. In some embodiments, maximizing the normalized cross correlation between the scan data and the embedding is configured to mitigate truncation artifacts.

According to a second aspect of the present technology, a non-transitory computer-readable medium storing instructions for causing a computing device to perform at least the following steps is provided: estimate a set of geometric parameters comprising the relative position of an x-ray source coupled to a source robotic arm, the relative position of an x-ray detector coupled to a detector robotic arm, and the relative angular orientation of the x-ray detector based on scan data received from the detector for a volume of interest (VOI) contained in an imaging object and utilizing a locally linear embedding (LLE) motion correction algorithm, wherein a set of weights for representing each of the set of geometric parameters is optimized by maximizing the normalized cross correlation between the scan data and its embedding; generate, via a reconstruction module, reconstructed image data from the estimated geometric parameters; and output corrected image data based, at least in part, on the reconstructed image data to form a corrected image of the VOI.

BRIEF DESCRIPTION OF DRAWINGS

The drawings show embodiments of the disclosed subject matter for the purpose of illustrating features and advantages of the disclosed subject matter. However, it should be understood that the present application is not limited to the precise arrangements and instrumentalities shown in the drawings, wherein:

FIG. 1 is a functional block diagram of a micro-CT apparatus according to an embodiment of the present technology.

FIG. 2 is a flow chart of operations for a method for correcting motion between an x-ray source and an x-ray detector according to an embodiment of the present technology.

FIG. 2(b) is a flow chart showing additional detail of some of the operations in FIG. 2(a).

FIG. 3 shows a visualization of a Jacobian matrix numerically calculated by introducing a tiny geometrical perturbation of 0.001 mm in translation and 0.0016 degree in rotation (simulated with a detector of 640 columns, 180 rows, and 0.444 mm×0.444 mm cell size at isocenter), and the rank of the matrix is 9 (full rank).

FIG. 4(a) shows an image of a digital head phantom;

FIG. 4(b) shows a truncated 2D projection generated from the phantom of FIG. 4(a);

FIG. 4(c) shows a compromised reconstruction of the phantom of FIG. 4(a) from truncated projections;

FIG. 4(d) shows a series of reprojections with the reconstruction of FIG. 4(c), each of which corresponds to a detector lateral misalignment;

FIG. 4(e) shows the curve of the root mean squared error measured between the original projection measurement and the reprojection views with respect to the detector lateral translation error;

FIG. 4(f) shows a plot of the normalized cross correlation measurement (normalized), unscaled correction measurement (unscaled), and direct correlation measurement (raw) against the detector lateral translation error;

FIG. 5 shows reconstructions of a truncated scan of a lithium-ion battery before (Original) and after detector drift correction through manual alignment (Manual), NCC-LLE according to one embodiment of the present technology, L2-LLE, Sun's earlier method based on gradient consistency (GDC), and Sun's latest method with LoG operation (GDC-LoG), obtained during a comparison study as described herein;

FIG. 6 shows zoom-in images of the region of interest in FIG. 5 with arrows pointing at positive electrode (left) and negative current collector (right).

FIG. 7 shows zoom-in sagittal images of the region of interest in FIG. 5 with circles and arrows marking the positive electrode and the negative current collector, respectively.

FIG. 8 shows a plot of the curves of root mean squared error (RMSE) between reprojections and measurements along iterations during geometrical error correction in the comparison study;

FIG. 9 shows a plot of estimations for detector drift along lateral (x) and vertical (z) directions with NCC-LLE correction according to one embodiment of the present technology, and in reference to manual alignment results with only lateral shift considered.

FIG. 10 shows the zoomed VOI in a sagittal slice before and after geometrical error correction via an embodiment of the present technology.

Although the following Detailed Description will proceed with reference being made to illustrative embodiments, many alternatives, modifications, and variations thereof will be apparent to those skilled in the art.

DETAILED DESCRIPTION

Generally, this disclosure relates to a robotic arm-based clinical micro-CT (CMCT) apparatus, method and/or system. It should be noted that a robotic arm-based clinical micro-CT apparatus, system and method, according to the present disclosure, may be utilized for numerous imaging applications, whether or not explicitly mentioned herein, within the scope of the present disclosure.

As used herein, medical CT corresponds to CT with a spatial resolution on the order of tenths of millimeters (mm). In one nonlimiting example, a medical CT image may have spatial resolution of 0.3 mm. The terms “medical CT”, “clinical CT” (without micro-) and/or “conventional CT” are used interchangeably. As used herein, “micro-CT” corresponds to CT with spatial resolution of the order of tens of micrometers (μm). As used herein, a “clinical micro-CT” corresponds to a micro-CT configured to image regions of a human body. In one nonlimiting example, a clinical micro-CT image may have a spatial resolution of 50 μm.

A robotic arm-based X-ray imaging system is configured with an X-ray source coupled to a first (“source”) robotic arm and an X-ray detector coupled to a second (“detector”) robotic arm in some embodiments. In some embodiments, the X-ray source includes, but is not limited to, a micro-focus X-ray tube, a dual energy CT source, e.g., a single-source X-ray source configured to emit an X-ray beam in two energy spectra, or a single energy spectrum source. In some embodiments, the X-ray detector includes, but is not limited to, an energy-integrating detector (EID), a current integrating detector (CID), a dual-layer detector, and a photon-counting detector (PCD). In one nonlimiting example, each robotic arm is configured with six degrees of freedom. Some embodiments of a robotic-arm-based X-ray imaging system, according to the present disclosure, provide flexibility in scanning and may facilitate a variety of scanning trajectories. The scanning trajectories can be task-specific and may include relatively diverse tasks targeting various organs and locations.

X-ray photon-counting detectors (PCDs), in some embodiments, enable relatively high-resolution (HR) and low-noise imaging, thus providing a spectral dimension to raw data and a corresponding improvement in CT performance. Different from an energy-integrating detector (EID), PCD works in a pulse-counting mode and directly converts individual X-ray photons into corresponding charge signals which are then sorted into different energy bins based on respective pulse heights. Thus, an intensity and wavelength information of incoming photons may be simultaneously obtained. Advantageously, PCDs generally do not suffer from electronic noise effects and may provide a relatively small effective pixel size; e.g., around 0.11 mm×0.11 mm and 0.055mm×0.055mm. As used herein, “around” and “approximately” correspond to within ±10 percent (%). PCDs allow applying selected weights to polychromatic photons for improved contrast and dose efficiency. Additionally or alternatively, an energy discrimination ability of PCDs may help reduce beam hardening and metal artifacts, and/or may enable K-edge imaging and material decomposition.

Micro-focus X-ray tubes are used with PCDs in micro-CT applications, according to some embodiments of the present disclosure. In one nonlimiting example, a microfocus X-ray tube includes electron emitting and receiving constructs (i.e., portions). The X-ray tube is configured to emit X-ray photons. The receiving portion contains an anode with a photoconductor. In some embodiments, the emission portion contains a backplate, a substrate, a cathode, a gate electrode, and an array of field emission electron sources. In another example, a microstructured array anode target (MAAT) X-ray source is configured to provide a relatively higher flux than an ordinary X-ray source in phase contrast imaging applications. It is contemplated that such technologies could be combined into a micro-focus X-ray tube for temporal bone CT imaging; for example, with a focal spot size of about 0.1 mm or less, corresponding to a PCD element size.

Generally, this disclosure relates to a robotic arm-based clinical micro-CT apparatus, method and/or system. The robotic arm-based clinical micro-CT apparatus, method and/or system, according to the present disclosure, may include a clinical micro-CT scanner. In an embodiment, the robotic arm-based clinical micro-CT apparatus includes the clinical micro-CT scanner and a computing device. In one embodiment, the clinical micro-CT scanner includes a micro-focus tube, and a PCD, each mounted on a robotic arm. In some embodiments, the clinical micro-CT apparatus, e.g., clinical micro-CT scanner, is configured to perform interior tomography. In some embodiments, the clinical micro-CT apparatus, e.g., computing device, may be configured to implement deep learning.

This disclosure also relates to motion correction with locally linear embedding for photon-counting computed tomography (CT) in some embodiments. A method, apparatus, system, and/or computer-readable medium containing software instructions may be configured to reduce or eliminate image artifacts that results from rigid-structure motion of the subject being imaged.

X-ray photon-counting detector (PCD) offers low noise, high resolution, and spectral characterization, representing a next generation of CT and enabling new biomedical applications. It is well known that involuntary patient motion may induce image artifacts with conventional CT scanning, and this problem becomes more serious with PCD due to its high-resolution detector pitch and extended scan time. Furthermore, there are few ways to target geometrical calibration of CT scans that include laterally truncated projections, for example interior tomography mode. For example, it is common to collect laterally truncated projections for oral and maxillofacial cone-beam CT. This data truncation issue invalidates most data consistency methods and also brings a great challenge to tomographic consistency-based motion estimation methods due to the truncation artifacts in the reconstruction.

Embodiments of the present disclosure are directed to a locally linear embedding (LLE) correction method, particularly as applied to robotic arm-based scanning systems, which is especially desirable given the high cost of large-area PCD. Embodiments of the present disclosure also perform incremental updating on gradually refined sampling grids for optimization of both accuracy and efficiency. As described below, however, instead of an L2-norm metric being used for optimization, a normalized cross-correlation (NCC) is used in some embodiments.

A rigid movement (translation and rotation) of a patient can be equivalently viewed as the relative movement of the X-ray source and detector pair around a stationary patient. Hence, both patient movement, coordination errors, and system misalignment can be taken as a view-specific geometric calibration problem. The goal is to estimate the geometry that maximizes the consistency between the projection measurements and the reprojections of the associated reconstruction.

Thus, for unified geometrical calibration in some embodiments, the geometrical errors for each CT projection view can be depicted with a 9 degrees of freedom (DOF) model to accommodate errors from all sources including system misalignment, coordination error, patient motion, etc. Specifically, the nominal geometry of a typical projection view can be denoted as $\{\boldsymbol{S}_0, \boldsymbol{D}_0, \boldsymbol{u}_0, \boldsymbol{v}_0\}$, where $\boldsymbol{S}_0, \boldsymbol{D}_0 \in \mathbb{R}^3$ represent the spatial positions of the source focal spot and the detector center, $\boldsymbol{u}_0, \boldsymbol{v}_0 \in \mathbb{S}^2$ are direction vectors of the detector row and column, $\boldsymbol{u}_0 \perp \boldsymbol{v}_0$, and $\mathbb{S}^2$ stands for the 3D unit sphere. The practical geometry $\{\boldsymbol{S}, \boldsymbol{D}, \boldsymbol{u}, \boldsymbol{v}\}$ can be fully described with translations of $\boldsymbol{S}_0$ and $\boldsymbol{D}_0$ characterized by $(st_x, st_y, st_z, dt_x, dt_y, dt_z)$ and rotations of $\boldsymbol{u}_0$ and $\boldsymbol{v}_0$ with $(\theta_x, \theta_y, \theta_z)$, where subscripts x, y, z represent the three Cartesian coordinate axes respectively. Thus, we have the geometrical misalignment vector $\boldsymbol{g}_i = [dt_x, dt_z, dt_y, \theta_x, \theta_y, \theta_z, st_x, st_z, st_y]^T$ for view i, where $i = 1, 2, \cdots, N_v$, and N_v is the total number of views. The geometrical misalignment compensation based on tomographic consistency can be formulated as the following optimization problem:

$$\underset{\boldsymbol{g},\boldsymbol{x}}{\arg\min} \|\boldsymbol{b} - A(\boldsymbol{g})\boldsymbol{x}\|_L \tag{1}$$

where $A(\cdot)$ is a system matrix as a function of the geometry parameters $\boldsymbol{g} = [\boldsymbol{g}_1, \cdots \boldsymbol{g}_i, \cdots, \boldsymbol{g}_{N_v}]^T$, $\boldsymbol{x}$ and $\boldsymbol{b}$ are the volumetric reconstruction and projection measurement respectively, and the distance between measurement and reprojection is measured by metric L. In some examples, the L2-norm is used as the metric to measure this projection domain difference.

The above optimization problem is often solved in some embodiments in an alternative updating manner between $\boldsymbol{g}$ and $\boldsymbol{x}$, and the two alternative steps are called motion update and image update respectively. Since the motion parameters for different views are separable between each other, the motion estimation can be performed view-wise during the motion update. One such sub-problem for a typical view can be formulated as

$$\boldsymbol{g}_i' = \underset{\boldsymbol{g}_i}{\arg\min} \|\boldsymbol{b}_i - A_i(\boldsymbol{g}_i)\boldsymbol{x}'\|_L \tag{2}$$

where $\boldsymbol{x}'$ is the reconstruction after the last image update, and $\boldsymbol{g}_i'$ is the currently estimated vector of motion parameters for view i.

In LLE-based optimization methods according to some embodiments, to solve Eq. 2, LLE densely samples a pre-defined parameter space and directly infers the solution from its nearest sampled points according to embedding theory (determined by metric values). The principle is that given a dense enough sampling grid, the true motion parameter $\boldsymbol{g}_i^*$ should be sufficiently close to its K-nearest neighbors in the grid such that both the low dimensional motion parameter $\boldsymbol{g}_i^*$ and corresponding high dimensional projection bi can be linearly embedded by their neighbors both of which share the same weights, i.e.,

$$\boldsymbol{g}_i^* = \sum_{k=1}^{K} w_k \boldsymbol{g}_i^{(k)}, \quad \boldsymbol{b}_i = \sum_{k=1}^{K} w_k \boldsymbol{p}_i^{(k)} \quad \text{s.t.} \quad \sum_{k=1}^{K} w_k = 1 \tag{3}$$

where $\boldsymbol{g}_i^{(k)}$ is one of the K nearest samples for $\boldsymbol{g}_i^*$ and $\boldsymbol{g}_i^* = A_i(\boldsymbol{g}_i^{(k)})\boldsymbol{x}'$ is the corresponding reprojection. Next, we have Eq. 3 assuming the full rank of the Jacobian matrix. Actually, due to the huge difference between the row dimension and the column dimension which are respectively the number of parameters in a motion vector and the number of pixel readings in a projection measurement, the full rank condition is normally satisfied in practice. One exemplary exceptional case is when projection images have uniform intensity such as an air scan, but those cases are rare due to rich structures/boundaries/shapes in the human anatomy or other samples to be scanned. FIG. 3 illustrates an exemplary Jacobian matrix of a cone-beam scan of a patient head showing strong sensitivity to the translations along the *x* (parallel to detector column direction here) and *z* (axial direction) axes, as well as the rotations around *y* (detector normal direction) and *z* axes. Thus, the full rank condition is easily met for this matrix of shape 9 × 115200.

A motion estimation algorithm, in some embodiments, for the view *i* can be formulated as follows:

1) Densely sample the parameter space with a grid $\left\{\boldsymbol{g}_i^{(j)} \middle| j = 1,\cdots, N_s\right\}$ where N_s is the number of sample points;

2) Calculate the reprojection grid at the above geometrical sampling points $\left\{(\boldsymbol{g}_i^{(j)}, \boldsymbol{p}_i^{(j)}) \middle| s = 1,\cdots, N_s\right\}$;

3) Identify K nearest neighbors $\left\{(\tilde{\boldsymbol{g}}_i^{(k)}, \tilde{\boldsymbol{p}}_i^{(k)}) \middle| k = 1,\cdots, K\right\}$ on the above reprojection grid to the measurement bi in terms of distance measured by metric L;

4) Embed $\boldsymbol{b}_i$ with the K nearest neighbors by solving the following optimization problem:

$$\tilde{\boldsymbol{w}} = \arg\min_{\boldsymbol{w}} \left\| \boldsymbol{b}_i - \sum_{k=1}^{K} w_k \tilde{\boldsymbol{p}}_i^{(k)} \right\|_L \text{ s.t.} \sum_{k=1}^{K} w_k = 1; \tag{4}$$

5) Update the estimation for $\boldsymbol{g}_i^*$ based on embedding weights $\tilde{\boldsymbol{w}}$ obtained above:

$$\boldsymbol{g}_i' = \sum_{k=1}^{K} \tilde{w}_k \tilde{\boldsymbol{g}}_i^{(k)}$$

In practice, densely sampling a multidimensional space can be rather expensive. In some embodiments, estimation for one parameter from $\boldsymbol{g}_i$ each time as an effective approximation is performed, i.e., via nine sequential 1D grid searches. After the motion parameters are updated for all views, the image reconstruction is updated. This process is repeated until convergence.

In some embodiments of the present technology, Equation 4 above is replaced with an equation based on a normalized cross correlation metric, instead of the $L2$-norm metric. While the $L2$-norm metric has been successfully applied in the LLE framework and proved effective for CT geometrical correction in several applications involving non-truncated CT scans, it is not equally effective or stable for interior tomography with LLE optimization. Similar results are observed using gradient-based optimization methods as well due to the data truncation problem.

In some embodiments, a normalized cross correlation-based embedding method is applied. Due to the insufficient measurement problem associated with the truncated data, the partial volume outside the VOI cannot be reconstructed well and appears blurry in the reprojection image. In some applications, the L2-norm does not differentiate well between feature-rich foreground and blurry background. On the other hand, in some embodiments, the cross-correlation metric captures more on fast changing fine structures in foreground and bypasses blurry background features, which is advantageous in many applications. Despite the improvement in accuracy and stability for interior tomography, the use of cross correlation embedding makes analytic-type reconstruction methods applicable to LLE-based geometrical error compensation. This greatly shortens the runtime as iterative reconstruction techniques are usually required for tomographic consistency type correction methods which can be the computational bottleneck for ultrahigh resolution CT imaging.

In some embodiments, the use of cross correlation-based embedding includes the following. With K neighbors $\{\boldsymbol{y}_j | j = 1,\cdots, K\}$ to embed the measured projection data (i.e., scan data) $\boldsymbol{y}_*$ with adjustable weighting coefficients $\boldsymbol{w} = [\boldsymbol{w}_1,\cdots,\boldsymbol{w}_j,\cdots,\boldsymbol{w}_K]^T$ to maximize the normalized cross correlation value between the embedding $\tilde{\boldsymbol{y}}$ and the measured projection data (i.e., scan data) $\boldsymbol{y}_*$. Mathematically, Eq. 4 is reformulated as the following optimization problem:

$$\arg\max_{w} \quad \frac{(\tilde{\boldsymbol{y}}^T - \tilde{\mu})(\boldsymbol{y}_* - \mu_*)}{\tilde{s}s_*} \quad s.t. \quad \tilde{\boldsymbol{y}} = [\boldsymbol{y}_1, \cdots, \boldsymbol{y}_K]\boldsymbol{w}, \ \sum_{j=1}^{K} w_j = 1, \tag{5}$$

$$\tilde{\mu} = \sum_{i=1}^{N} \tilde{\boldsymbol{y}}_{[i]}/N, \tilde{s} = \sqrt{\sum_{i=1}^{N} (\tilde{\boldsymbol{y}}_{[i]} - \tilde{\mu})^2/(N-1)} \tag{6}$$

where μ_*, s_* and $\tilde{\mu}$, $\tilde{s}$ are the mean and standard deviation for the measured projection $\boldsymbol{y}_*$ and its embedded representation $\tilde{\boldsymbol{y}}$, $\boldsymbol{y}_{[i]}$ indexes elements of $\boldsymbol{y}$, and N corresponds to the total number of sample points.

To simplify the normalized cross correlation objective in Eq. 5, the normalized measured projection signal $\boldsymbol{y}_*^n$ is defined as $(y_* - \mu_*)/s_*$. The mean and standard deviation values for each embedding basis $\boldsymbol{y}_j$ are denoted as μ_j and s_j, $j = 1,\cdots,K$, and the normalized basis as $y_j^n = (y_j - \mu_j)/s_j$. Then, $\tilde{\mu}$ can be expressed as:

$$\tilde{\mu} = \sum_{i=1}^{N} \sum_{j=1}^{j=K} w_j\, \boldsymbol{y}_{j[i]}/N = \sum_{j=1}^{K} w_j \sum_{i=1}^{i=N} \boldsymbol{y}_{j[i]}/N = \sum_{j=1}^{K} w_j\, \mu_j \tag{7}$$

Similarly, $\tilde{s}$ can be simplified as:

$$\tilde{s}^2 = \sum_{i=1}^{N} (\sum_{j=1}^{j=K} w_j\, \boldsymbol{y}_{j[i]} - \tilde{\mu})^2/(N-1)$$

$$= \sum_{i=1}^{N} (\sum_{j=1}^{j=K} w_j\, \boldsymbol{y}_{j[i]} - w_j\mu_j)^2/(N-1)$$

$$= \sum_{i=1}^{N} (\sum_{j=1}^{j=K} w_j\, \boldsymbol{y}_{j[i]} - w_j\mu_j)(\sum_{j'=1}^{j'=K} w_{j'}\, \boldsymbol{y}_{j'[i]} - w_{j'}\mu_{j'})/(N-1)$$

$$= \sum_{j'=1}^{j'=K} \sum_{j=1}^{j=K} w_j\, w_{j'} s_j s_{j'} (\boldsymbol{y}_j^n)^T \boldsymbol{y}_{j'}^n/(N-1)$$

$$= \sum_{j'=1}^{j'=K} \sum_{j=1}^{j=K} w_j\, w_{j'} s_j s_{j'} \boldsymbol{r}_{[j,j']}$$

where $\boldsymbol{r}$ is the correlation matrix among the bases, and $s_j s_{j'} \boldsymbol{r}_{[j,j']}$ represents the covariance between basis $\boldsymbol{y}_{j'}$ and $\boldsymbol{y}_j$. As shown here, $\tilde{s}$ is the weighted sum of the covariance matrix of the bases, serving as a scaling factor to normalize the magnitude in Eq. 5. Without loss of generality, we only use the weighted sum of the diagonal values from the covariance matrix to serve the same purpose and simplify the optimization problem,

$$\tilde{s}^2 \cong \sum_{j=1}^{K} w_j^2 s_j^2 \tag{8}$$

Based on the above, the normalized embedding $\tilde{\boldsymbol{y}}^n$ can be expressed as

$$\tilde{\boldsymbol{y}}^n = \frac{\sum_{j=1}^{K} w_j(y_j-\mu_j)}{\sqrt{\sum_{j=1}^{K} w_j^2 s_j^2}} = \sum_{j=1}^{K} \frac{w_j s_j}{\sqrt{\sum_{j=1}^{K} w_j^2 s_j^2}} (\frac{y_j-\mu_j}{s_j}) \tag{9}$$

Thus, the objective function can be reformulated as

$$\underset{\boldsymbol{w}}{argmax} (\tilde{\boldsymbol{y}}^n)^T \boldsymbol{y}_*^n = \underset{\boldsymbol{w}}{argmax} \sum_{j=1}^{K} \frac{w_j s_j}{\sqrt{\sum_{j=1}^{K} w_j^2 s_j^2}} \left(\left(\boldsymbol{y}_j^n\right)^T \boldsymbol{y}_*^n \right) \tag{10}$$

The correlation between each basis and the scan data is a constant for the optimization over $\boldsymbol{w}$, and denoted as $c_j, j = 1,\cdots, K$.The optimization problem is then simplified as

$$\underset{\boldsymbol{w}}{argmax} \sum_{j=1}^{K} \frac{w_j s_j c_j}{\sqrt{\sum_{j=1}^{K} w_j^2 s_j^2}} \; s.t. \sum_{j=1}^{K} w_j = 1 \tag{11}$$

By introducing the auxiliary variable $w_j' = w_j s_j$, the objective function can be expressed in the following form:

$$\underset{\boldsymbol{w}}{argmax} \sum_{j=1}^{K} \frac{w_j'}{\sqrt{\sum_{j=1}^{K} w_j'^2}} c_j \;\; s.t. \sum_{j=1}^{K} w_j'/s_j = 1 \tag{12}$$

which has a geometrical meaning that to find a point $\boldsymbol{w}'$ on the plane $\boldsymbol{s}^T\boldsymbol{w}' = 1$ with its direction (starting from the origin) $\boldsymbol{w}'/\| \boldsymbol{w}' \|$ maximally aligned with the given vector $\boldsymbol{c}$, where $s = \left[\frac{1}{s_1},\cdots,\frac{1}{s_K}\right]^T$ and $c = [c_1,\cdots,c_K]^T$. Clearly, s_j is non-negative by definition. Also, $c_i$should be non-negative due to the neighboring selection. Then, the vector c or its extension should intersect the plane, and the cross-point will be the solution $\boldsymbol{w}' = \boldsymbol{c}/\boldsymbol{s}^T\boldsymbol{c}$. That is, we have the solution for the original optimization problem as follows:

$$\boldsymbol{w} = \frac{[c_1/s_1, \cdots, c_K/s_K]^T}{\sum_{j=1}^{K} c_j/s_j} \tag{13}$$

FIG. 1 illustrates a functional block diagram of an apparatus 100 that includes a motion correction system 101 for motion correction for photon-counting CT, according to several embodiments of the present disclosure. Apparatus 100 further includes a photon-counting CT scanner 102 for imaging an imaging object 108. Photon-counting CT scanner 102 includes an X-ray source 140 coupled to a source robotic arm 141 and a photon counting detector (PCD) 142 coupled to a detector robotic arm 143. In some embodiments, the robotic arms 141 and 143 each provide six degrees of freedom for positioning each of the X-ray source and the detector relative to one another in space. In other embodiments, fewer degrees of freedom are utilized for one or both of the robotic arms.

The imaging object 108 includes a volume of interest (VOI) 146, which is the apparatus's target for imaging. The VOI can be any suitable portion of a human or animal body, or any other object suitable for imaging via CT. Motion correction system 101 includes, in some embodiments, computing device 106, which includes motion correction circuitry 120. The motion correction circuitry includes a motion correction algorithm configured to reduce or eliminate image artifacts that result from patient movement, system misalignment, coordination errors, etc.

Motion correction circuitry 120 includes logic, in the form of software instructions in several embodiments, configured to receive the measured projection data (also referred to as scan data) 107 from the photon-counting CT scanner 102 and perform an LLE motion correction algorithm, as discussed above. In some embodiments, the LLE motion correction algorithm includes estimating a set of geometric parameters comprising the relative position of the x-ray source, the relative position of the x-ray detector, and the relative angular orientation of the x-ray detector based on the scan data of the VOI. In some embodiments, "relative" is relative to a nominal positioning. In some embodiments, the LLE motion correction algorithm includes wherein a set of weights for representing each of the set of geometric parameters is optimized by maximizing the normalized cross correlation between the scan data and its embedding. In some embodiments, maximizing the normalized cross correlation between the scan data and the embedding is configured to mitigate truncation artifacts.

In some embodiments, because each of the robotic arms provides full and free movement of the source and detector in space, and because the detector can have an angular adjustment, the apparatus has nine degrees of freedom to be accounted for by the LLE motion correction algorithm. The nine geometric parameters are: the relative position of the x-ray source is defined by three source coordinates in three-dimensional space (st_x, st_z, st_y), the relative position of the x-ray detector is defined by three detector coordinates in three-dimensional space (dt_x, dt_z, dt_y), and the relative angular position of the x-ray detector As defined by three rotation angles (θ_x, θ_y, θ_z), each rotation angle relative to a respective axis of the three-dimensional space.

In some embodiments, the LLE motion correction algorithm comprises software instructions for estimating each of the nine geometric parameters by performing the following steps for each parameter: generating a sampling grid for the parameter having N sample points; calculating forward projections corresponding to the samples on the sampling grid; finding the K projections on the projection grid for each scan data point associated with the sampling grid that are the nearest neighbors to the scan data point; optimizing the weights for the K neighbors using equations 5 and 6, above, where $\boldsymbol{w}$ corresponds to the weight vector, $\boldsymbol{y}_*$

is the measured projection, $\tilde{\boldsymbol{y}}$ is the embedding, μ_*, s_* and $\tilde{\mu}$, $\tilde{s}$ are the mean and standard deviation for the measured projection $\boldsymbol{y}_*$ and its embedded representation $\tilde{\boldsymbol{y}}$, and $\boldsymbol{y}_{[i]}$ indexes elements of $\boldsymbol{y}$; and updating the estimated parameter and image reconstruction. These steps are iterated until a convergence is reached for each parameter or terminated early for a specified number of iterations for each parameter.

In some embodiments, the weights are calculated using equation 12, where c_j corresponds to the correlation between each embedding basis $\boldsymbol{y}_j$ and the measured projection data, and s_j is the standard deviation value for each embedding basis $\boldsymbol{y}_j$. In some embodiments, the estimate for each geometric parameter is obtained using the following equation:

$$\boldsymbol{g}_i' = \sum_{k=1}^{K} \tilde{w}_k \tilde{\boldsymbol{g}}_i^{(k)}$$

where $\boldsymbol{g}_i'$ is the estimated geometric parameter in the form of a vector $[dt_x, dt_z, dt_y, \theta_x, \theta_y, \theta_z, st_x, st_z, st_y]^T$, and $\boldsymbol{g}_i^{(k)}$ are the K neighbors of $\boldsymbol{g}_i'$.

Reconstruction module 122 includes logic configured to receive the motion correction data 130 (including the geometric parameters) outputted from the LLE motion correction algorithm and generate reconstructed image data, which is used to generate corrected image data 109 to form a corrected image of the VOI.

Computing device 106 may include, but is not limited to, a computing system (e.g., a server, a workstation computer, a desktop computer, a laptop computer, a tablet computer, an ultraportable computer, an ultramobile computer, a netbook computer and/or a subnotebook computer, etc.), and/or a smart phone. Computing device 106 includes a processor 110, a memory 112, input/output (I/O) circuitry 114, a user interface (UI) 116, and data store 118.

Processor 110 is configured to perform processing operations of apparatus 100. Memory 112 may be configured to store data associated with apparatus 104. I/O circuitry 114 may be configured to provide wired and/or wireless communication functionality for apparatus 100. For example, I/O circuitry 114 may be configured to receive measured correction data 107 and to provide corrected image data 109. UI 116 may include a user input device (e.g., keyboard, mouse, microphone, touch sensitive display, etc.) and/or a user output device, e.g., a display. Data store 118 may be configured to store one or more of measured correction data 107, corrected image data 109, and/or other data associated with any part of apparatus 100.

FIG. 2a is a flowchart 200 of operations for a method of motion correction for photon-counting CT, according to various embodiments of the present disclosure. In particular, the flowchart 200 illustrates a method for correcting motion between an x-ray source coupled to a source robotic arm and an x-ray detector coupled to a detector robotic arm. The operations may be performed, for example, by the system 100 of FIG.1.

Operations of this embodiment begin with scanning a subject's VOI via a photon-counting CT scanner device to obtain measured projection data, or scan data, at operation 202. Operation 204 includes estimating a set of geometric parameters associated with the source and detector from the measured projection data using a locally linear embedding (LLE) motion correction algorithm. Operation 206 includes generating, via reconstruction circuitry, reconstructed image data from the estimated geometric parameters. Operation 208 includes outputting corrected image data based, at least in part, on the reconstructed image data to form a corrected image of the VOI. Although the operations of motion correction method are shown in flowchart 200 in a certain order, this is not meant to limit operations of the motion correction method to that specific order. For example, embodiments of the present disclosure may perform operations in any suitable order.

FIG. 2b is a flow chart showing details of the process for estimating the geometric parameters and updating the reconstructions for each view to arrive at a final reconstruction according to an embodiment. To begin, the projection measurement and an initial geometry estimation is input at step 210. Then, for each parameter of the nine geometric parameters, a sample grid is generated having N sample points at step 211. Then, forward projections corresponding to the samples on the sampling grid are calculated at step 212. Then, the K projections on the projection grid for each scan data point associated with the sampling grid that are the nearest neighbors to the scan data point are found at step 213. Then, the weights for the K neighbors are optimized, using equations 5 and 6 at step 214. Then, the estimated parameter and image reconstruction is updated at step 215. The above steps are iterated until a convergence or a specified number of iterations is reached for each parameter at step 216. Finally, the final reconstruction is made at step 217.

Thus, a method, according to the present disclosure, may be configured to reduce or eliminate image artifacts that results from rigid-structure motion of the subject being imaged by utilizing an LLE-based motion correction method for helical photon-counting CT, which decomposes the motion correction problem into each and every view with respect to individual parameters, and works iteratively in a highly parallel manner. Embodiments of the present disclosure exclude bad photon-counting detector pixels, and utilize unreliable volume masking, incremental updating, and incrementally refined gridding techniques synergistically. Thus, major improvements have been made in accuracy and efficiency of motion estimation and correction.

<u>Cross-Correlation Illustration</u>

FIG. 4 illustrates the NCC metric between projection measurement and the misalignment-involved reprojections with respect to detector lateral shifts. The interior reconstruction (Fig. 4(c)) of a digital head phantom (Fig. 4(a)) from the projection measurement (Fig. 4(b)) with a detector of a limited field of view presents strong artifacts due to the lateral projection truncations. By introducing different amounts of misalignment errors to the detector lateral position, the magnitude of reprojection errors relative to the original measurement changes accordingly. In this case, the root mean square error (RMSE) metric is still able to reflect the change of misalignment error with measurements on projection intensity difference as shown in Fig. 4(e), which is the foundation for the convergence of the $L2$-norm-based LLE methods. Similarly, with the correlation-based metrics the similarity between two intensity spatial distributions (or the directions) is measured rather than the simple intensity differences.

The curves of the correlation-based metrics are displayed in Fig 4(f), where ‘raw’ denotes direct cross correlation measurements without bias or gain correction (i.e., $\tilde{\boldsymbol{y}}^T \boldsymbol{y}_*$), ‘unscaled’ means that with only bias correction (i.e., $(\tilde{\boldsymbol{y}}^T - \tilde{\mu})(\boldsymbol{y}_* - \mu_*)$), and ‘normalized’ represents the metric as depicted in Eq. 5. Due to the truncation artifacts, there could be positive low-frequency components in the reprojections which undermine the direct correlation measurement with the bright patches in the image, as illustrated by the ‘raw’ curve. Similarly, the gain should also be corrected to mitigate artifacts’ influence as illustrated by the ‘unscaled’ curve. With only normalized cross correlation, the similarity as a function of misalignment error can be correctly measured. The monotonic trend of the normalized curve with respect to the misalignment error magnitude serves as the foundation for the convergence of the NCC-LLE method.

<u>Experiments</u>

An embodiment of an NCC-LLE method was applied using a high-resolution micro-CT scan of a lithium-ion battery from Apple AirPods (ear-bud style headphones). The scan consisted of 3,601 projection frames covering one full rotation of the sample. Each frame consisted of 2, 304 × 2, 940 pixels with a pitch size of 49.5 μm. The source to object distance was 15.000 mm while the source to detector is 886.740 mm. During the scan, the detector was drifted, which caused double edge artifacts in reconstructed images. Without loss of generalizability, the problem was scaled down by down-sampling the projections by half and taking the central 150 rows as a test scan. The volume was reconstructed with 5.1μm voxel size into a volume of 73 × 724 × 724 voxels in the image updating stage using the ordered subset simultaneous iterative reconstruction technique (OSSIRT). In this experiment, the 2D translational movements of the detector were considered. After correction, the volume was reconstructed using the FDK algorithm for the final results.

For NCC-LLE misalignment correction, the incremental update framework was followed with coarse-to-fine sampling steps. The searching range was initially 9.9 mm and 1.98 mm for lateral and vertical shift respectively and then decayed by a factor of 0.7 after each iteration. 5 iterations were performed in total and sample grid size kept at 51 (lateral) and 17 (vertical) during the whole process.

For comparison, the method developed for truncated situations by Sun et al in 2021 for dental cone beam CT was used ("A motion correction approach for oral and maxillofacial cone-beam ct imaging," Physics in Medicine & Biology, vol. 66, no. 12, p. 125008, 2021), as well as an earlier version (T. Sun, J.-H. Kim, R. Fulton, and J. Nuyts, "An iterative projection-based motion estimation and compensation scheme for head x-ray ct," Medical physics, vol. 43, no. 10, pp. 5705–5716, 2016). These methods are also based on tomographic consistency. Under this method, it is theorized that, with a close enough geometry estimation, (1) the reprojection should match the measurement (tomographic consistency); and (2) the derivative of the projection on the pose parameters numerically calculated in different ways should match (gradient consistency), i.e. calculated at the ground truth point and calculated at the estimation point. Based on that idea, a least square minimization problem is constructed for parameter estimation. For this comparison, the multi-scale and patch-based reconstruction were not implemented for fair comparison since they are for image update acceleration. σ was set = 1 and a kernel size of 5×5 for the Laplacian of Gaussian ("LoG") operation was used, and δr = 0.1mm (lateral) and δr = 0.02mm (vertical) for the earlier gradient consistency version and δr = 0.297mm (lateral) and δr = 0.059mm (vertical) for the latest gradient consistency with LoG operations version.

An $L2$-norm-based LLE method was also performed with the same settings as NCC-LLE as a baseline comparison.

<u>Results</u>

FIG. 5 displays the FDK reconstruction result of the scan before any correction, after manual alignment, after correction with the NCC-LLE method, after correction with the L2-norm-based LLE method (L2-LLE), after correction with Sun’s earlier version of gradient consistency method (GDC), and after correction with Sun’s latest method with LoG operation (GDC-LoG). Significant truncation artifacts are observed in all reconstructions due to lateral truncation of the projection measurement since the detector can only cover a small portion of the battery sample. Serious double-edge artifacts are observed in the original reconstruction before any correction, and after manual alignment most double-edge artifacts are mitigated within the volume of interest (VOI) indicated by the bright ring of truncation artifacts though residual double-edges can be still seen outside the VOI. NCC-LLE successfully removes all double-edges both within and outside the VOI and provides sharpest contrast. L2-LLE and GDC methods seem to correct the double-edges very well outside the VOI but struggle at some regions within VOI. In contrast, GDC-LoG is focused more within VOI though it looks worse than L2-LLE and GDC.

FIG. 6 is the zoom-in image of VOI corresponding to FIG. 5 and provides a better look at the VOI with more details. The arrows point to representative structures in a typical lithium-ion battery, i.e., the positive electrode and negative current collector. In this embodiment, the NCC-LLE eliminates all double-edge artifacts resulting the best contrast of structures. For example, looking at the negative current collector pointed by the arrow on the right-hand side, the double edges in the original reconstruction are significantly narrowed after manual alignment but the residuals are still noticeable; L2-LLE and GDC further improve at some segments but struggle at other segments presenting strong artifacts; and, GDC-LoG performed the worst unexpectedly. Another example is the positive electrode indicated by the arrow on the left side of the images, the brightness and the clearness of its boundary reflect the blurriness or image contrast. The NCC-LLE method presents the best contrast compared to others. Interestingly, the manual alignment improves the double-edge artifacts but its image looks blurrier than others.

FIG. 7 shows the sagittal view of the reconstruction VOI. The circle and arrow marks the positive electrode and negative current collector respectively. Similar results are observed compared to FIG. 6. The NCC-LLE method shows the best contrast and the least residual double-edge artifacts. The residual double-edge artifacts are more noticeable in sagittal view for manual alignment. New observations are that L2-LLE and GDC methods present ghost images at the top and bottom ends while others do not. Since the original reconstruction does not present similar ghost shadows, this implies the ghost shadows were produced by L2-LLE and GDC algorithms and suggesting the instability of L2 measurements for truncated scans. Most interestingly, GDC-LoG method achieves the second best image quality despite some residual artifacts near the arrow in this time, which suggests the effects of LoG operation in improving L2-metric for consistency measurement.

FIG 8 presents the root mean squared error measured in projection domain during the correction iterations of different methods. NCC-LLE, L2-LLE, and GDC methods were performed for 5 iterations while GDC-LoG was continued for 10 iterations till convergence. It appears that L2-LLE method reduces the reprojection error the most, however, the correction performance is the worst in the sagittal views. The GDC method shows similar results. This suggests that L2 metric may not be the most effective way to measure the consistency for interior tomography with truncated projections due to the truncation artifacts. In addition, the NCC-LLE method converges very fast within 2 iterations, and is significantly faster than the GDC-LoG method which takes 6 iterations. Considering the iterative reconstruction being the runtime bottle neck for high-resolution imaging, NCC-LLE is also computationally more efficient (required 1.25 hours for 2 iterations) than the GDC-LoG method (took 2.72 hours for 6 iterations) in addition to the improved accuracy.

FIG. 9 shows the detector drift estimation results obtained with NCC-LLE method in reference to the manual estimation which only considers lateral shifts. The high-frequency serrations on the drifting curves show the ability of our methods to address non-smooth geometrical errors. On the other hand, considering the good reconstruction quality after correction, the serrations could be realistic, which suggests the necessity of non-dependence to non-smooth assumptions for high-resolution imaging.

In an additional exemplary experiment, a robotic CT scan of a euthanized mouse with unknown misalignment and coordination errors was taken. FIG. 10 shows that sharper images with clearer anatomical details were obtained after our geometric calibration. FIG. 10 shows the zoomed VOI in a sagittal slice before and after geometrical error correction via an embodiment of the present technology.

As used in any embodiment herein, the terms “logic” and/or “module” may refer to an app, software, firmware and/or circuitry configured to perform any of the aforementioned operations. Software may be embodied as a software package, code, instructions, instruction sets and/or data recorded on non-transitory computer readable storage medium. Firmware may be embodied as code, instructions or instruction sets and/or data that are hard-coded (e.g., nonvolatile) in memory devices.

“Circuitry,” as used in any embodiment herein, may include, for example, singly or in any combination, hardwired circuitry, programmable circuitry such as computer processors comprising one or more individual instruction processing cores, state machine circuitry, and/or firmware that stores instructions executed by programmable circuitry. The logic and/or module may, collectively or individually, be embodied as circuitry that forms part of a larger system, for example, an integrated circuit (IC), an application-specific integrated circuit (ASIC), a system on-chip (SoC), desktop computers, laptop computers, tablet computers, servers, smart phones, etc.

Memory 112 may include one or more of the following types of memory: semiconductor firmware memory, programmable memory, non-volatile memory, read only memory, electrically programmable memory, random access memory, flash memory, magnetic disk memory, and/or optical disk memory. Either additionally or alternatively system memory may include other and/or later-developed types of computer-readable memory.

Embodiments of the operations described herein may be implemented in a computer-readable storage device having stored thereon instructions that when executed by one or more processors perform the methods. The processor may include, for example, a processing unit and/or programmable circuitry. The storage device may include a machine readable storage device including any type of tangible, non-transitory storage device, for example, any type of disk including floppy disks, optical disks, compact disk read-only memories (CD-ROMs), compact disk rewritables (CD-RWs), and magneto-optical disks, semiconductor devices such as read-only memories (ROMs), random access memories (RAMs) such as dynamic and static RAMs, erasable programmable read-only memories (EPROMs), electrically erasable programmable read-only memories (EEPROMs), flash memories, magnetic or optical cards, or any type of storage devices suitable for storing electronic instructions.

The terms and expressions which have been employed herein are used as terms of description and not of limitation, and there is no intention, in the use of such terms and expressions, of excluding any equivalents of the features shown and described (or portions thereof), and it is recognized that various modifications are possible within the scope of the claims. Accordingly, the claims are intended to cover all such equivalents.

Various features, aspects, and embodiments have been described herein. The features, aspects, and embodiments are susceptible to combination with one another as well as to variation and modification, as will be understood by those having skill in the art. The present disclosure should, therefore, be considered to encompass such combinations, variations, and modifications.

CLAIMS

What is claimed is:

1. A computed tomography (CT) apparatus, comprising:

an x-ray source;

an x-ray detector adapted to output scan data of a volume of interest (VOI) contained in an imaging object; and

a computing device, comprising:

a motion correction circuitry, comprising software instructions for:

estimating a set of geometric parameters comprising the relative position of the x-ray source, the relative position of the x-ray detector, and the relative angular orientation of the x-ray detector based on the scan data, wherein relative is relative to nominal, and utilizing a locally linear embedding (LLE) motion correction algorithm, wherein a set of weights for representing each of the set of geometric parameters is optimized by maximizing the normalized cross correlation between the scan data and its embedding;

generating, via a reconstruction module, reconstructed image data from the estimated geometric parameters; and

outputting corrected image data based, at least in part, on the reconstructed image data, to form a corrected image of the VOI.

2. The apparatus of claim 1, wherein the maximizing the normalized cross correlation between the scan data and the embedding is configured to mitigate truncation artifacts.

3. The apparatus of claim 2, wherein there are nine geometric parameters per view: the relative position of the x-ray source is defined by three source coordinates in three-dimensional space (st_x, st_z, st_y), the relative position of the x-ray detector is defined by three detector coordinates in three-dimensional space (dt_x, dt_z, dt_y), and the relative angular position of the x-ray detector is defined by three rotation angles (θ_x, θ_y, θ_z), each rotation angle relative to a respective axis of the three-dimensional space.

4. The apparatus of claim 3, wherein the LLE motion correction algorithm comprises software instructions for:

estimating each of a set of geometric parameters by, for each parameter:

generating a sampling grid for the parameter having N sample points;

calculating forward projections corresponding to the samples on the sampling grid;

finding the K projections on the projection grid for each scan data point associated with the sampling grid that are the nearest neighbors to the scan data point;

optimizing the weights for the K neighbors using the equation

$$\arg\max_{\boldsymbol{w}} \quad \frac{(\tilde{\boldsymbol{y}}^T - \tilde{\mu})(\boldsymbol{y}_* - \mu_*)}{\tilde{s}s_*} \quad s.t. \quad \tilde{\boldsymbol{y}} = [\boldsymbol{y}_1, \cdots, \boldsymbol{y}_K]\boldsymbol{w}, \ \sum_{j=1}^{K} w_j = 1$$

$$\tilde{\mu} = \sum_{i=1}^{N} \tilde{\boldsymbol{y}}_{[i]}/N, \tilde{s} = \sqrt{\sum_{i=1}^{N} (\tilde{\boldsymbol{y}}_{[i]} - \tilde{\mu})^2/(N-1)},$$

where $\boldsymbol{w}$ corresponds to the weight vector, $\boldsymbol{y}_*$ is the scan data, $\tilde{\boldsymbol{y}}$ is the embedding, μ_*, s_* and $\tilde{\mu}$, $\tilde{s}$ are the mean and standard deviation for the scan data $\boldsymbol{y}_*$ and its embedded representation $\tilde{\boldsymbol{y}}$, and $\boldsymbol{y}_{[i]}$ indexes elements of $\boldsymbol{y}$;

updating the estimated parameter and image reconstruction; and

iterating the above steps until a convergence or a specified number of iterations is reached for each parameter.

5. The apparatus of claim 4, wherein the weights are calculated using the equation:

$$\boldsymbol{w} = \frac{[c_1/s_1, \cdots, c_K/s_K]^T}{\sum_{j=1}^{K} c_j/s_j}$$

where c_j corresponds to the correlation between each embedding basis $\boldsymbol{y}_j$ and the scan data, and s_j is the standard deviation value for each embedding basis $\boldsymbol{y}_j$.

6. The apparatus of claim 5, wherein the estimate for each geometric parameter is obtained using the following equation:

$$\boldsymbol{g}'_i = \sum_{k=1}^{K} \tilde{w}_k \tilde{\boldsymbol{g}}_i^{(k)}$$

where $\boldsymbol{g}_i'$ is the estimated geometric parameter in the form of a vector $[dt_x, dt_z, dt_y, \theta_x, \theta_y, \theta_z, st_x, st_z, st_y]^T$, and $\boldsymbol{g}_i^{(k)}$ are the K neighbors of $\boldsymbol{g}_i'$.

7. The apparatus of claim 3, wherein for each iteration a sampling space for the sampling grid is reduced while maintaining the same number of samples to generate a finer sample grid.

8. A non-transitory computer-readable medium storing instructions for causing a computing device to:

estimate a set of geometric parameters comprising the relative position of an x-ray source, the relative position of an x-ray detector, and the relative angular orientation of an x-ray detector based on scan data received from the detector for a volume of interest (VOI) contained in an imaging object, wherein relative is relative to nominal, and utilizing a locally linear embedding (LLE) motion correction algorithm, wherein a set of weights for representing each of the set of geometric parameters is optimized by maximizing the normalized cross correlation between the scan data and its embedding;

generate, via a reconstruction module, reconstructed image data from the estimated geometric parameters; and

output corrected image data based, at least in part, on the reconstructed image data, to form a corrected image of the VOI.

9. The medium of claim 8, wherein the maximizing the normalized cross correlation between the scan data and the embedding is configured to mitigate truncation artifacts.

10. The medium of claim 9, wherein there are nine geometric parameters per view: the relative position of the x-ray source is defined by three source coordinates in three-dimensional space (st_x, st_z, st_y), the relative position of the x-ray detector is defined by three detector coordinates in three-dimensional space (dt_x, dt_z, dt_y), and the relative angular position of the x-ray detector is defined by three rotation angles (θ_x, θ_y, θ_z), each rotation angle relative to a respective axis of the three-dimensional space.

11. The medium of claim 10, wherein the LLE motion correction algorithm comprises instructions to:

estimate each of the nine geometric parameters by, for each parameter:

generating a sampling grid for the parameter having N sample points;

calculating forward projections corresponding to the samples on the sampling grid;

finding the K projections on the projection grid for each scan data point associated with the sampling grid that are the nearest neighbors to the scan data point;

optimizing the weights for the K neighbors using the equation

$$\arg\max_{\boldsymbol{w}} \quad \frac{(\tilde{\boldsymbol{y}}^T - \tilde{\mu})(\boldsymbol{y}_* - \mu_*)}{\tilde{s}s_*} \quad s.t. \quad \tilde{\boldsymbol{y}} = [\boldsymbol{y}_1, \cdots, \boldsymbol{y}_K]\boldsymbol{w}, \sum_{j=1}^{K} w_j = 1$$

$$\tilde{\mu} = \sum_{i=1}^{N} \tilde{\boldsymbol{y}}_{[i]}/N, \tilde{s} = \sqrt{\sum_{i=1}^{N} (\tilde{\boldsymbol{y}}_{[i]} - \tilde{\mu})^2/(N-1)},$$

where $\boldsymbol{w}$ corresponds to the weight vector, $\boldsymbol{y}_*$ is the scan data, $\tilde{\boldsymbol{y}}$ is the embedding, μ_*, s_* and $\tilde{\mu}$, $\tilde{s}$ are the mean and standard deviation for the scan data $\boldsymbol{y}_*$ and its embedded representation $\tilde{\boldsymbol{y}}$, and $\boldsymbol{y}_{[i]}$ indexes elements of $\boldsymbol{y}$;

updating the estimated parameter and image reconstruction; and

iterating the above steps until a convergence or a specified number of iterations is reached for each parameter.

12. The medium of claim 11, wherein the weights are calculated using the equation:

$$\boldsymbol{w} = \frac{[c_1/s_1, \cdots, c_K/s_K]^T}{\sum_{j=1}^{K} c_j/s_j}$$

where c_j corresponds to the correlation between each embedding basis $\boldsymbol{y}_j$ and the scan data, and s_j is the standard deviation value for each embedding basis $\boldsymbol{y}_j$.

13. The medium of claim 12, wherein the estimate for each geometric parameter is obtained using the following equation:

$$\boldsymbol{g}_i' = \sum_{k=1}^{K} \tilde{w}_k \tilde{\boldsymbol{g}}_i^{(k)}$$

where $\boldsymbol{g}_i'$ is the estimated geometric parameter in the form of a vector $[dt_x, dt_z, dt_y, \theta_x, \theta_y, \theta_z, st_x, st_z, st_y]^T$, and $\boldsymbol{g}_i^{(k)}$ are the K neighbors of $\boldsymbol{g}_i'$.

13. The medium of claim 11, wherein for each iteration a sampling space for the sampling grid is reduced while maintaining the same number of samples to generate a finer sample grid.

14. A method for correcting motion between an x-ray source coupled to a source robotic arm and an x-ray detector coupled to a detector robotic arm, comprising the steps of:

estimating a set of geometric parameters comprising the relative position of an x-ray source, the relative position of an x-ray detector, and the relative angular orientation of an x-ray detector based on scan data received from the detector for a volume of interest (VOI) contained in an imaging object, wherein relative is relative to nominal, and utilizing a locally linear embedding (LLE) motion correction algorithm, wherein a set of weights for representing each of the set of geometric parameters is optimized by maximizing the normalized cross correlation between the scan data and its embedding;

generating, via a reconstruction module, reconstructed image data from the estimated geometric parameters; and

outputting corrected image data based, at least in part, on the reconstructed image data, to form a corrected image of the VOI.

15. The method of claim 14, wherein the maximizing the normalized cross correlation between the scan data and the embedding is configured to mitigate truncation artifacts.

16. The method of claim 15, wherein there are nine geometric parameters per view: the relative position of the x-ray source is defined by three source coordinates in three-dimensional space (st_x, st_z, st_y), the relative position of the x-ray detector is defined by three detector coordinates in three-dimensional space (dt_x, dt_z, dt_y), and the relative angular position of the x-ray detector is defined by three rotation angles $(\theta_x, \theta_y, \theta_z)$, each rotation angle relative to a respective axis of the three-dimensional space.

16. The method of claim 15, wherein the step of estimating further comprises estimating each of the nine geometric parameters by, for each parameter:

generating a sampling grid for the parameter having N sample points;

calculating forward projections corresponding to the samples on the sampling grid;

finding the K projections on the projection grid for each scan data point associated with the sampling grid that are the nearest neighbors to the scan data point;

optimizing the weights for the K neighbors using the equation

$$\arg\max_{\boldsymbol{w}} \quad \frac{(\tilde{\boldsymbol{y}}^T - |\tilde{\mu})(\boldsymbol{y}_* - \mu_*)}{\tilde{s}s_*} \quad s.t. \quad \tilde{\boldsymbol{y}} = [\boldsymbol{y}_1, \cdots, \boldsymbol{y}_K]\boldsymbol{w}, \sum_{j=1}^{K} w_j = 1$$

$$\tilde{\mu} = \sum_{i=1}^{N} \tilde{\boldsymbol{y}}_{[i]}/N, \tilde{s} = \sqrt{\sum_{i=1}^{N} (\tilde{\boldsymbol{y}}_{[i]} - \tilde{\mu})^2/(N-1)},$$

where $\boldsymbol{w}$ corresponds to the weight vector, $\boldsymbol{y}_*$ is the scan data, $\tilde{\boldsymbol{y}}$ is the embedding, μ_*, s_* and $\tilde{\mu}$, $\tilde{s}$ are the mean and standard deviation for the scan data $\boldsymbol{y}_*$ and its embedded representation $\tilde{\boldsymbol{y}}$, and $\boldsymbol{y}_{[i]}$ indexes elements of $\boldsymbol{y}$; and

updating the estimated parameter and image reconstruction; and

iterating the above steps until a convergence or a specified number of iterations is reached for each parameter.

17. The method of claim 16, wherein the weights are calculated using the equation:

$$\boldsymbol{w} = \frac{[c_1/s_1, \cdots, c_K/s_K]^T}{\sum_{j=1}^{K} c_j/s_j}$$

where c_j corresponds to the correlation between each embedding basis $\boldsymbol{y}_j$ and the scan data, and s_j is the standard deviation value for each embedding basis $\boldsymbol{y}_j$.

18. The method of claim 17, wherein the estimate for each geometric parameter is obtained using the following equation:

$$\boldsymbol{g}_i' = \sum_{k=1}^{K} \tilde{w}_k \tilde{\boldsymbol{g}}_i^{(k)}$$

where $\boldsymbol{g}'_i$ is the estimated geometric parameter in the form of a vector $[dt_x, dt_z, dt_y, \theta_x, \theta_y, \theta_z, st_x, st_z, st_y]^T$, and $\boldsymbol{g}_i^{(k)}$ are the K neighbors of $\boldsymbol{g}'_i$.

19. The method of claim 16, further comprising the step of reducing a sampling space for the sampling grid for each iteration while maintaining the same number of samples to generate a finer sample grid.

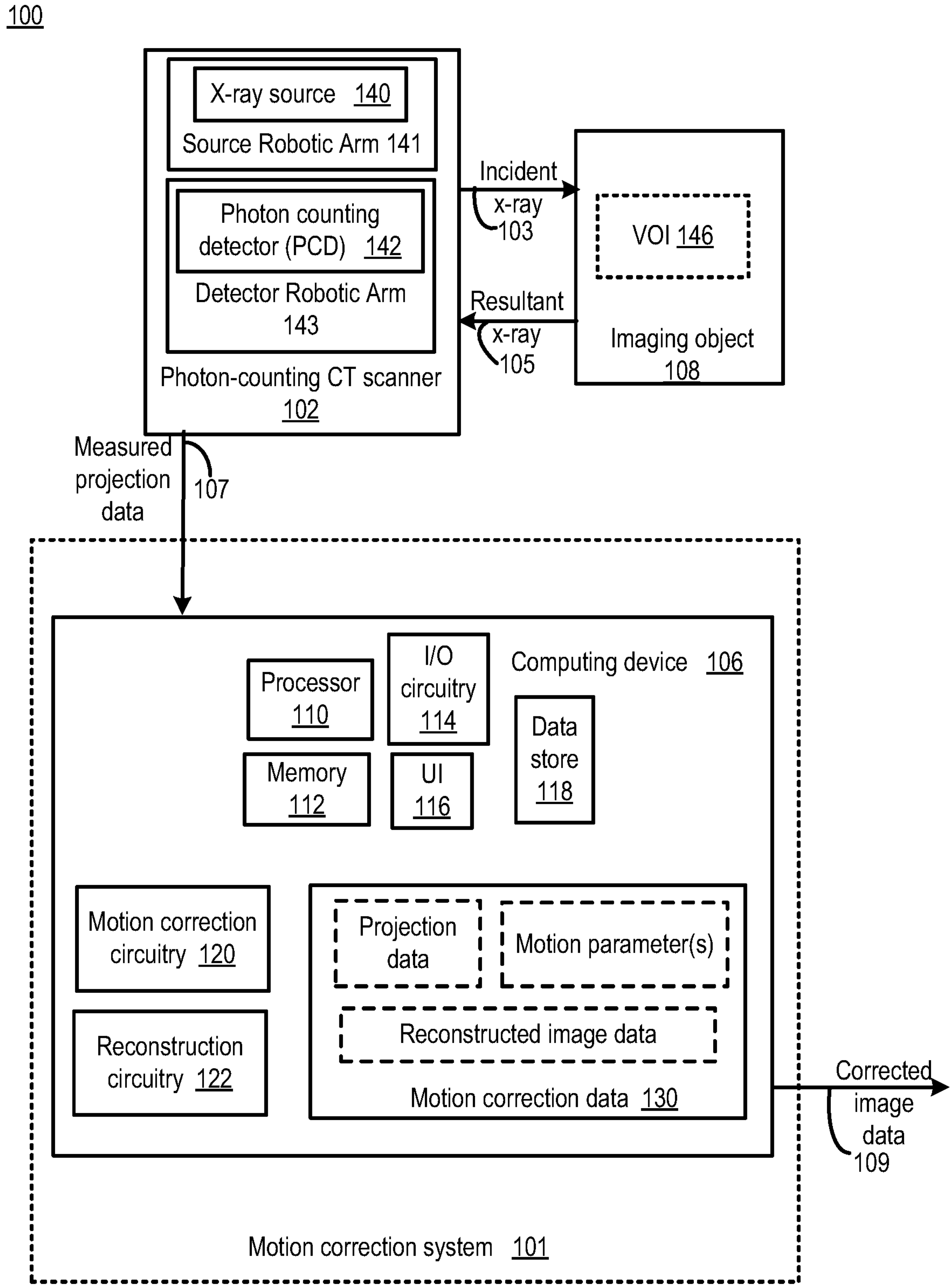
100
X-ray source 140
Source Robotic Arm 141
Photon counting detector (PCD) 142
Detector Robotic Arm 143
Photon-counting CT scanner 102
Incident x-ray 103
Resultant x-ray 105
VOI 146
Imaging object 108
Measured projection data
107
Processor 110
I/O circuitry 114
Computing device 106
Memory 112
UI 116
Data store 118
Motion correction circuitry 120
Reconstruction circuitry 122
Projection data
Motion parameter(s)
Reconstructed image data
Motion correction data 130
Corrected image data
109
Motion correction system 101

FIG. 1

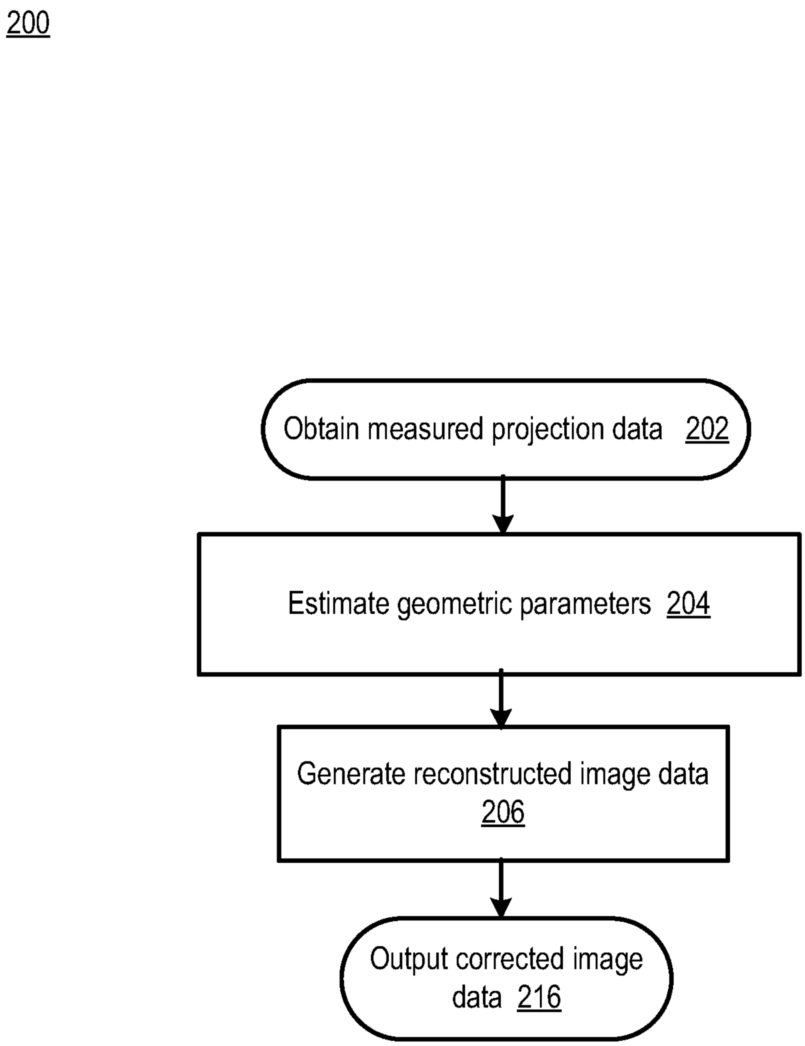
200
Obtain measured projection data 202
Estimate geometric parameters 204
Generate reconstructed image data 206
Output corrected image data 216

FIG. 2a

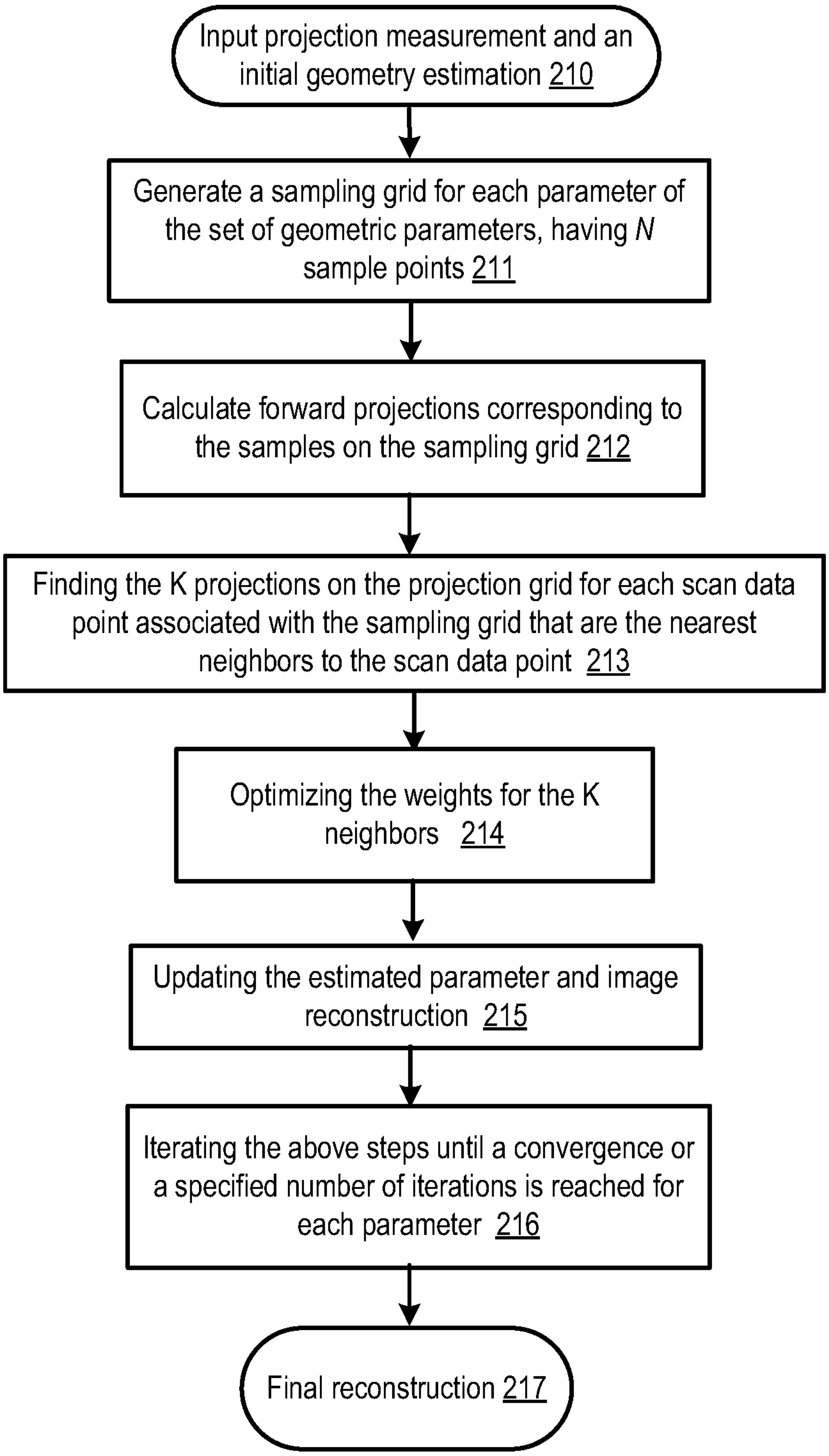
Input projection measurement and an initial geometry estimation 210
Generate a sampling grid for each parameter of the set of geometric parameters, having N sample points 211
Calculate forward projections corresponding to the samples on the sampling grid 212
Finding the K projections on the projection grid for each scan data point associated with the sampling grid that are the nearest neighbors to the scan data point 213
Optimizing the weights for the K neighbors 214
Updating the estimated parameter and image reconstruction 215
Iterating the above steps until a convergence or a specified number of iterations is reached for each parameter 216
Final reconstruction 217

FIG. 2b

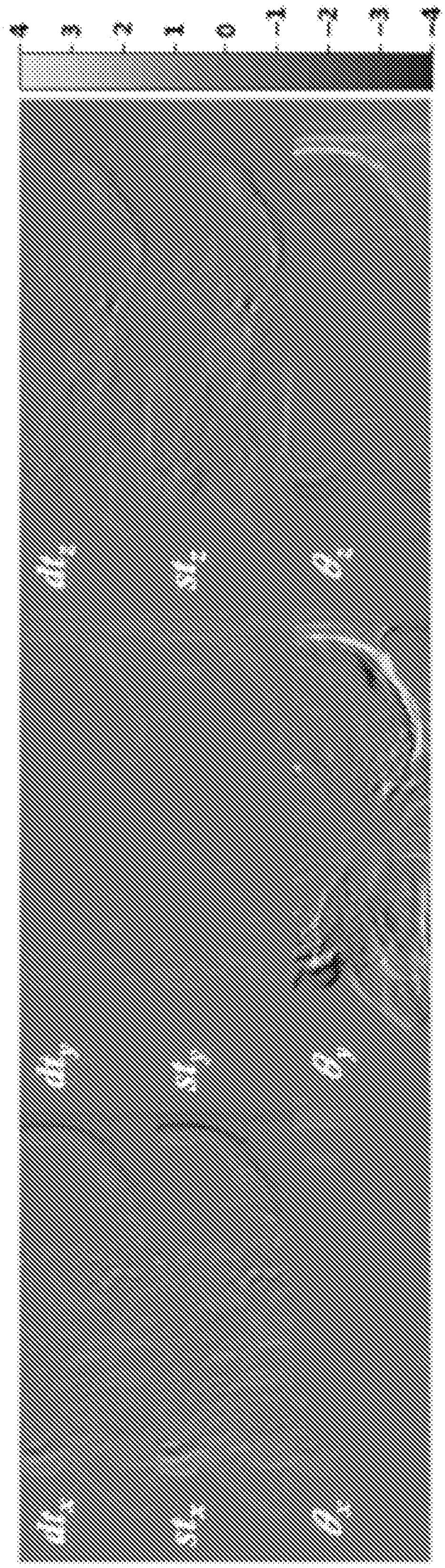

FIG. 3

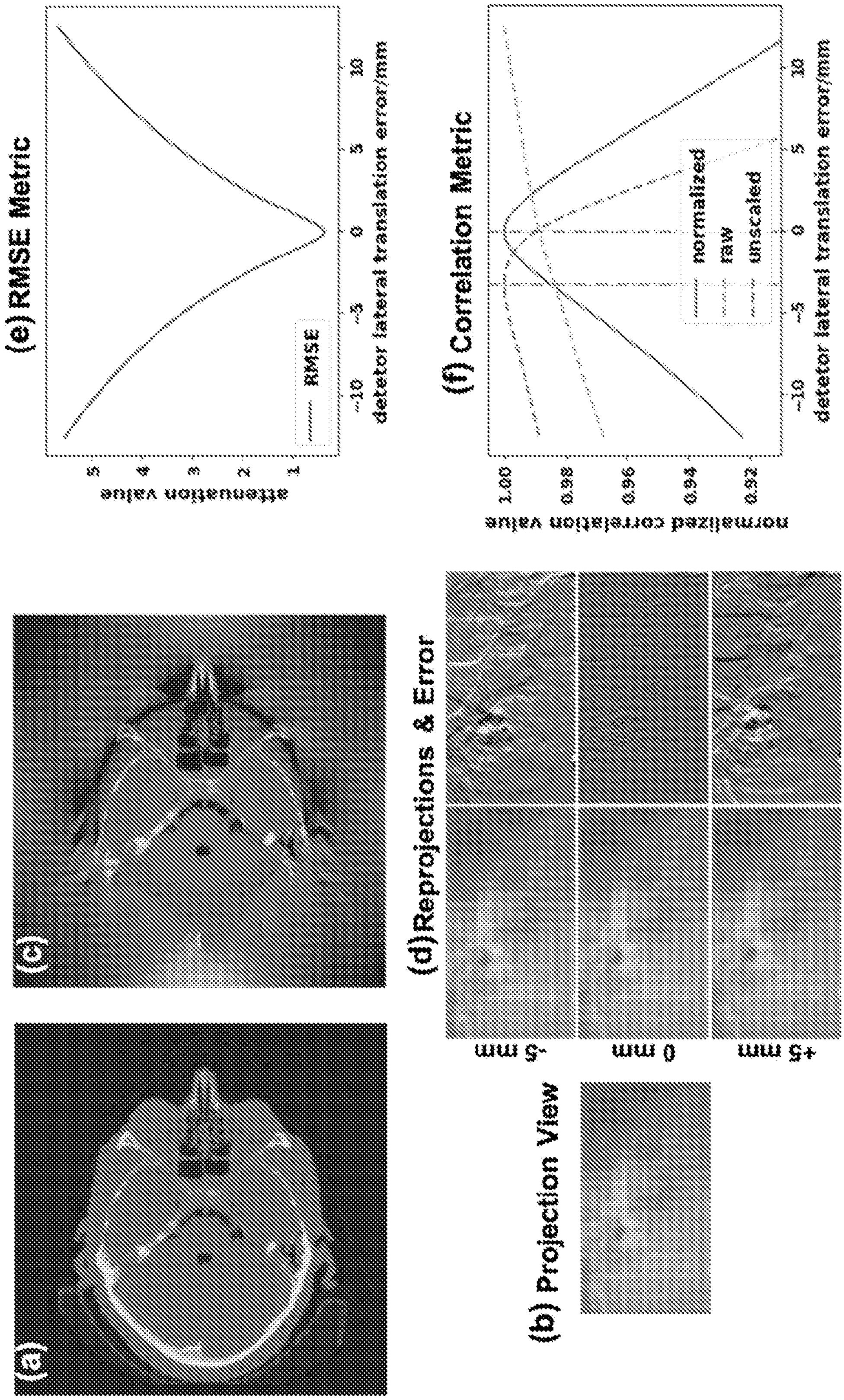
(a)
(b) Projection View
(c)
(d) Reprojections & Error
-5 mm
0 mm
+5 mm
(e) RMSE Metric
RMSE
attenuation value
detetor lateral translation error/mm
(f) Correlation Metric
normalized
raw
unscaled
normalized correlation value
detetor lateral translation error/mm

FIG. 4

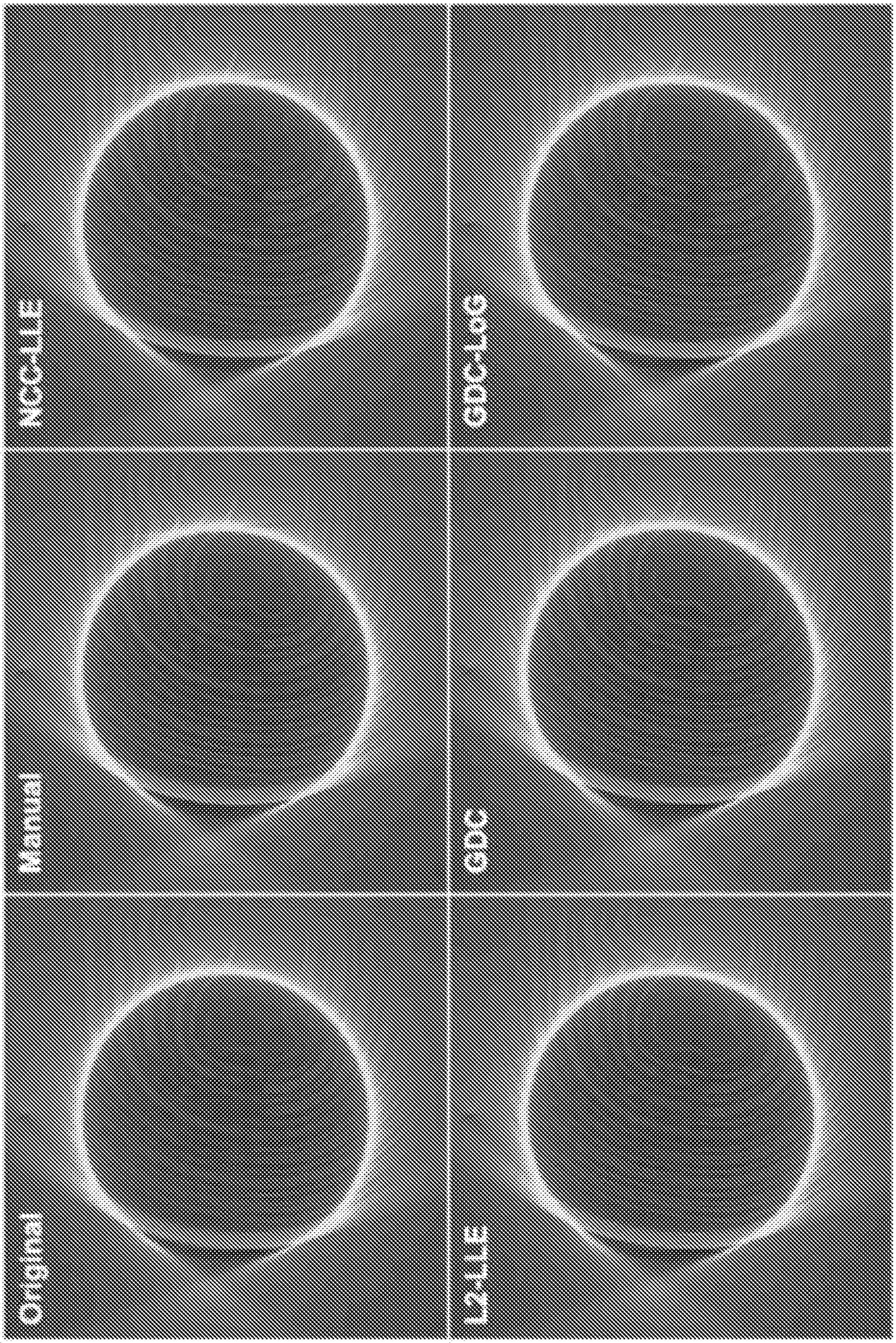

FIG. 5

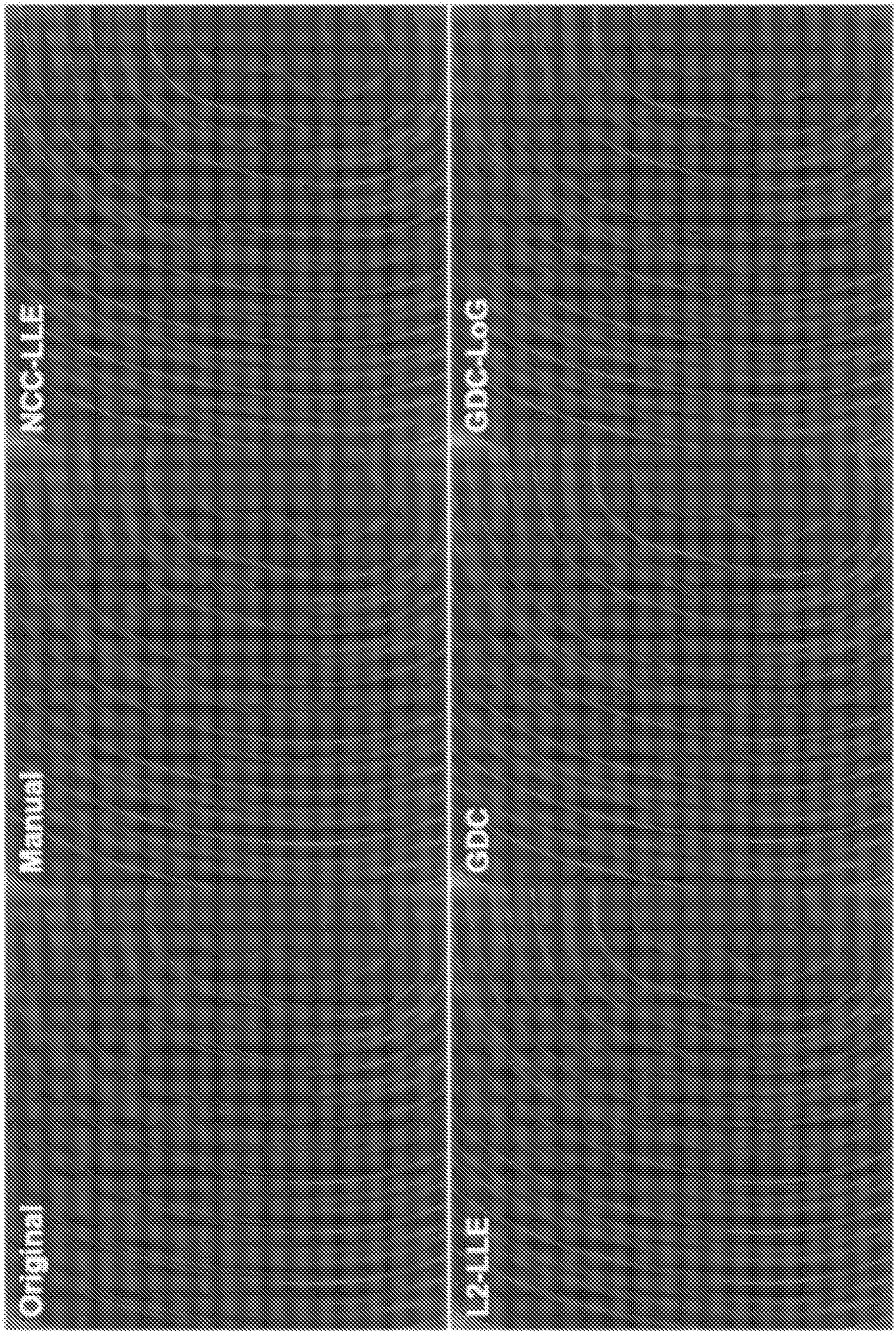

FIG. 6

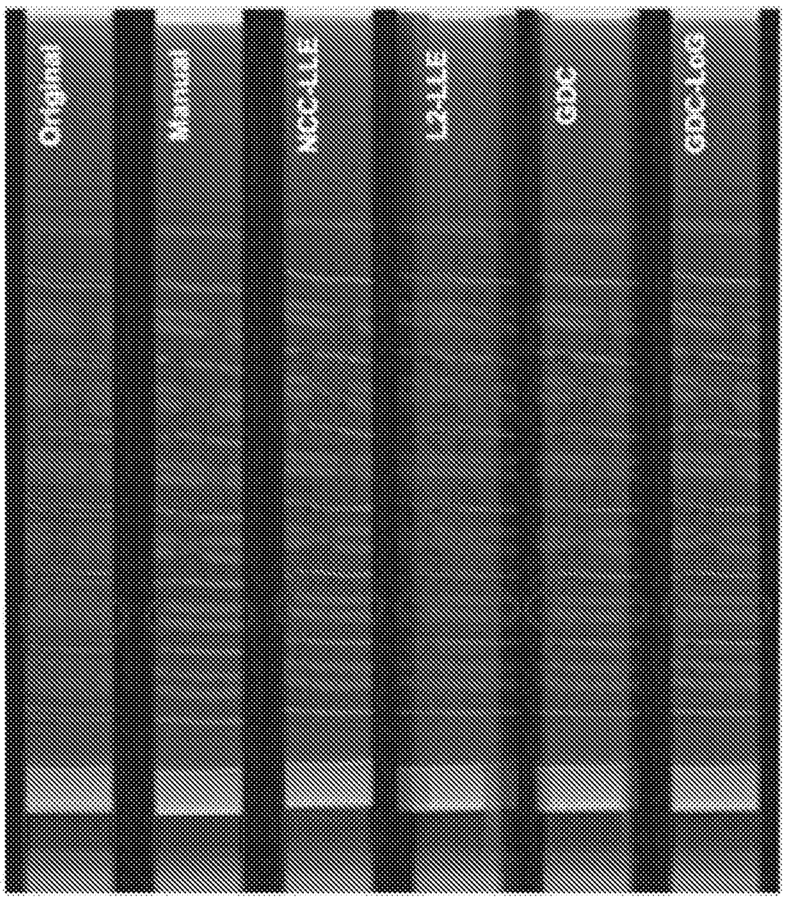

FIG. 7

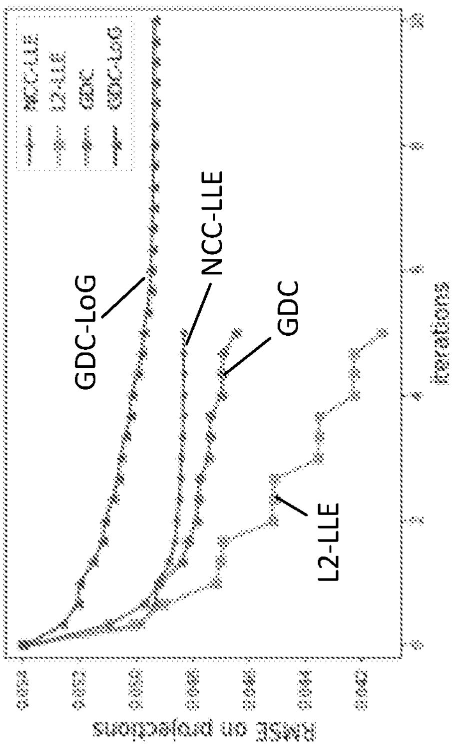

FIG. 8

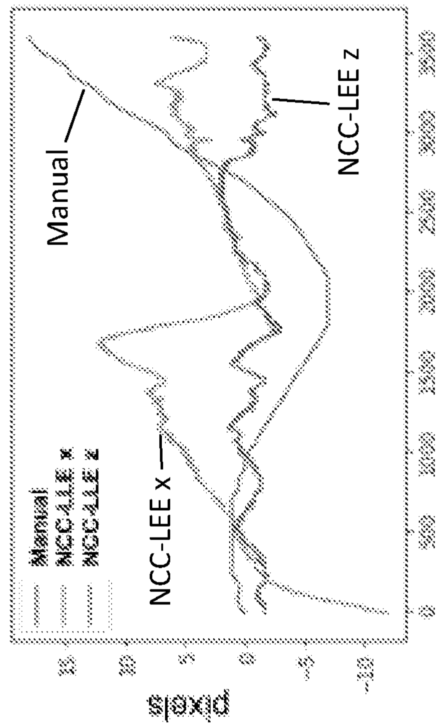

FIG. 9

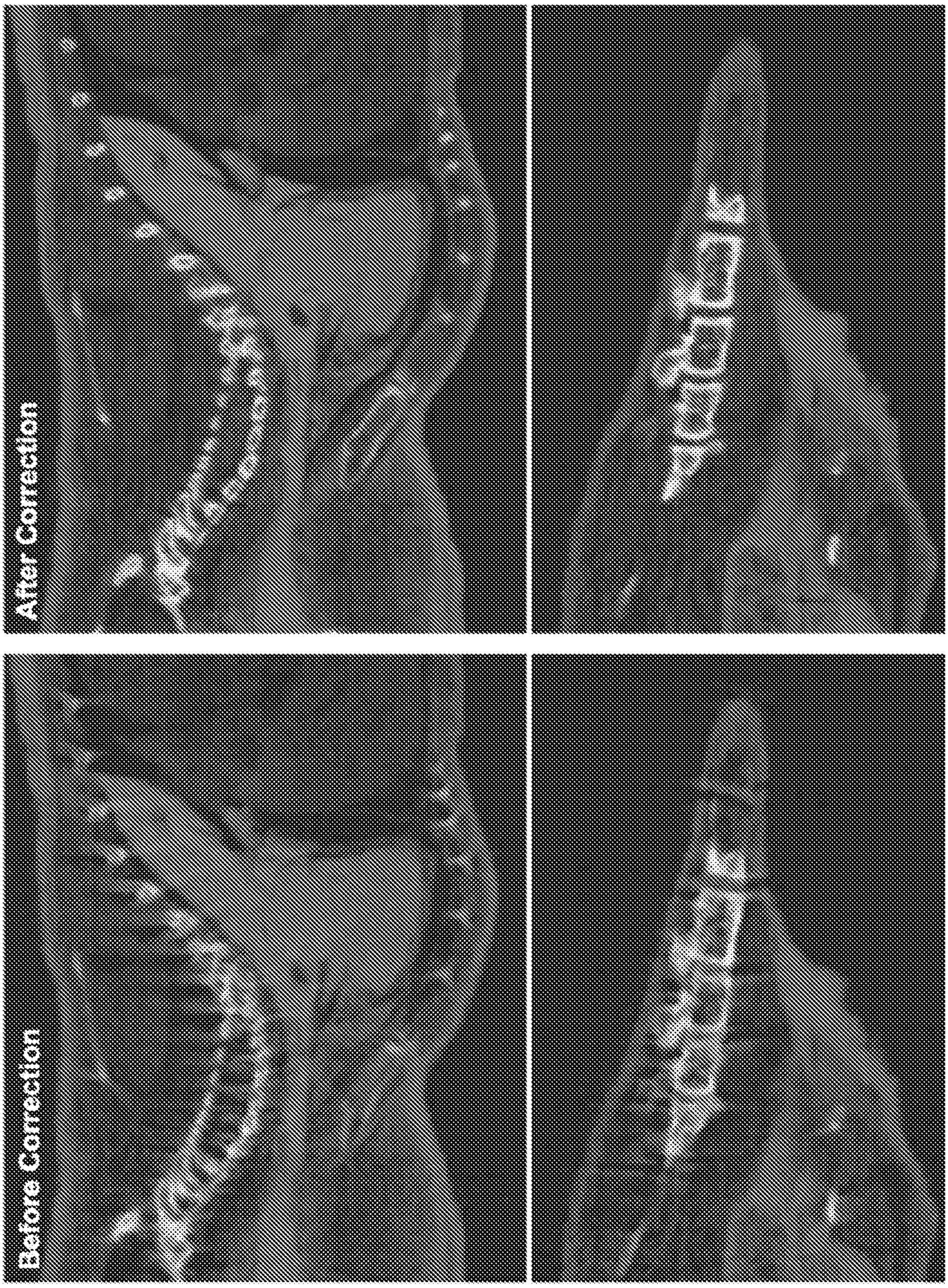

FIG. 10